



Final Draft **of the original manuscript**

Paul, H.; Chulist, R.; Mania, I.; Schell, N.; Lityńska-Dobrzyńska, L.:
**Interfacial Reactions in the Bonding Zones of Explosively
Welded Tantalum to Stainless Steel Sheets.**

In: Advanced Engineering Materials. Vol. 23 (2021) 11, 2001521.

First published online by Wiley: 11.03.2021

<https://dx.doi.org/10.1002/adem.202001521>

Interfacial reactions in the bonding zones of explosively welded tantalum to stainless steel sheets

H. Paul^{1*}, R. Chulist¹, I. Mania¹, N. Schell², L. Lityńska-Dobrzyńska¹

¹Institute of Metallurgy and Materials Science, Polish Academy of Sciences, 25 Reymonta St., 30-059 Krakow, Poland

²Institute of Materials Research, Helmholtz-Zentrum Geesthacht, Max-Planck-Strasse 1, D-21502 Geesthacht, Germany

h.paul@imim.pl (H.P.), r.chulist@imim.pl, i.mania@imim.pl, norbert.schell@hzg.de, l.litynska@imim.pl

* Correspondence (H.P.): h.paul@imim.pl; Tel.: +48-295-28-33

Abstract

The microstructure of the interfacial layers of explosively welded Ta/stainless steel (SS) and Ta/Cu/SS composites were investigated by X-ray synchrotron radiation, scanning (SEM) and transmission (TEM) electron microscopies. SEM analyses showed that all interfaces between joined sheets underwent wave-shaped deformation with the solidified melt regions situated preferentially in the wave vortexes and at the wave crests. These reaction regions show a non-uniform distribution of phases in terms of chemical composition with elements belonging to both neighboring sheets. According to TEM analyses and synchrotron X-ray measurements the solidified melt regions between Ta and SS predominantly consist of brittle, amorphous or nano-crystalline phases that are not observed in equilibrium phase diagrams. The microstructure of the solidified melt near the Ta/Cu interface is dominated by Cu and Ta nanoparticles and small dendrites, typically less than 100 nm in diameter, while nano-sized crystalline phases with complex chemical compositions were identified near the Cu/SS interface.

Keywords: Explosion welding, Tantalum/stainless steel and Tantalum/Copper/stainless steel composites, Synchrotron radiation, SEM & TEM, Solidified melt regions

1. Introduction

Tantalum (Ta) is one of the best corrosion-resistant materials for most corrosive situations [1-3]. However, the major limitation to the wider use of Ta is its high cost. This causes restrictions to large-scale industrial applications, such as chemical process pressure vessels, electrode plate drums, columns, heat exchanger tube sheets or bonnets, etc. [1]. It is hence highly advisable to use thin Ta sheets (<2 mm) as a coating on load-bearing stainless (SS) or carbon (CS) steels. Such bi-metallic composites allow to combine the exceptional high corrosion resistance of Ta and high strength of SS or CS base materials [3]. However, a large difference in melting points of steel and Ta (Ta: 3293 K and Fe: 1811 K) makes their joining very difficult. Currently, explosive welding (EXW) is the only efficient way of surface joining Ta and steel sheets into a compact metallic composite [4-8].

EXW is a phenomenon of materials joining that occurs during the collision of two or more similar or dissimilar metallic materials under a very high pressure coming from controlled detonation of an explosive charge, e.g. [4, 5]. After igniting the explosive charge, the detonation wave propels the upper (flyer) sheet towards the bottom (base) plate (Fig. 1). During this

process, the flyer sheet initially bends then collapses on the base plate. As a result of an oblique collision, a plasma jet (a stream of heated gases) forms at the collision line. During the temperature rise period, the heat of the plasma jet together with the impact energy and the plastic work dissipated to heat, leads to local melting [6]. During solidification (cooling period), the molten volumes undergo extremely rapid cooling. This leads to significant microstructural changes in the interfacial layers, mainly due to the formation of solidified melt regions of various chemical compositions and structures [9-14]. They strongly influence the strength properties of the clad.

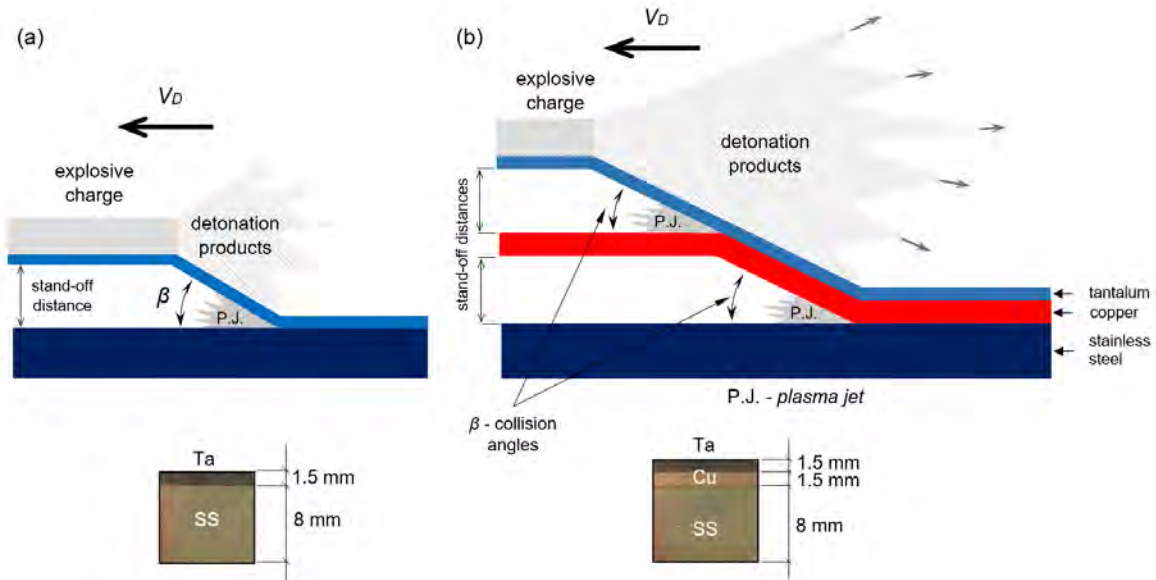


Fig. 1. (a) Schematic presentation of EXW: (a) bi-layered (Cu/SS) and, (b) tri-layered (Ta/Cu/SS) composites formation and corresponding final structures. (V_D - detonation velocity).

Joining technology based on the direct bonding of Ta sheet with steel plate causes several problems. These problems are associated with the formation of undesirable brittle intermetallics and difficulties with butt weld joints during further clad processing [4]. For example, if one attempts to join Ta to steel with fusion welding, the melted regions (of near the eutectic composition) transform upon solidification into brittle intermetallics. This deteriorates significantly the strength properties of the composite [1]. To solve these problems, soft and high thermal conductivity copper (Cu) sheet, as an intermediate layer, can be used [15-19].

According to equilibrium binary phase diagrams of Cu-Ta [20] and Cu-Fe [21, 22], for both pairs, the metals are soluble in each other above the liquidus temperatures. However, between liquidus and solidus lines, a miscibility gap exists in these systems. The Cu and Ta are practically immiscible over the whole range of temperatures. The copper and iron, meanwhile, are immiscible only at room temperature and noticeable mutual solubility is observed at higher temperatures. For these reasons, it is particularly intriguing to investigate the effect of the intermediate copper layer on the structural properties of solidified melt regions in Ta/Cu/SS clads.

The microstructure and the phase composition of interfacial layers of Ta-based clads have received little attention to date. Only a few works provide information about manufacturing procedure [1, 8] or the influence of EXW conditions on the bond strength and structure of the interfacial layers [4, 6-8, 15-17, 23-28]. They refer to: Ta/CS [1, 4], Ta/Cu [16, 17, 24-28], Ta/Al [28], Ta/stainless steel [8, 15, 17]. Among them only Paul et al. [7, 15, 24], Bataev et al.

[6], Yang et al. [8], Lysak et al. [23] and Greenberg et al. [28] used scanning (SEM) and/or transmission (TEM) electron microscopy analyses to characterize the structure of melted regions. To our best knowledge, there have been no reports concerning in detail the microstructure, phase, and chemical compositions of the reaction regions in copper to steel clads, despite strong interest in Cu/SS composites, e.g. [25, 29, 30].

In this study a detailed characterization of microstructure, crystal structure, and chemical composition of the reaction regions of EXW Ta/SS and Ta/Cu/SS clads is shown. They have been carried out by means of TEM, SEM, and high-energy synchrotron radiation. The evaluation of the strength properties of the reaction regions *via* microhardness measurements supported these analyses.

2. Experimental

Tantalum, oxygen-free copper (M1E), and 304 L stainless steel sheets/plates were selected for clads preparation. The chemical compositions of the flyer, intermediate, and base sheets/plates are presented in Table 1. A stainless steel plate with a thickness of 8 mm was used as the base plate, a copper sheet with a thickness of 1.5 mm as an intermediate layer, whereas a tantalum sheet with a thickness of 1.5 mm as the flyer sheet. The sheet/plate size was $440 \times 210 \text{ mm}^2$. Metallic supports (stand-off distances between sheets/plates) with a height of 2 mm (Fig. 1), were used for clad preparation. A mixture of ammonium nitrate and fuel oil (ANFO) with a charge density of $750 \text{ kg}\cdot\text{m}^{-3}$ was used as an explosive charge. The explosive was evenly distributed over the surface of the flyer sheet with a detonator located in the middle of its shorter edge. These conditions led to detonation velocities (V_D) of $2550 \text{ m}\cdot\text{s}^{-1}$ (Ta/Cu/SS) and $2600 \text{ m}\cdot\text{s}^{-1}$ (Ta/SS). EXW process was performed with a parallel arrangement of sheets/plates.

Table 1. Chemical composition of joined components (wt. %)

Tantalum (<i>Hamilton Precision Metals® certificate</i>)												
Chemical element	C	O	N	H	Ni	Ti	W	Mo	Sn	Ta		
wt.%	0,01	0,015	0,01	0,0015	0,1	0,1	0,05	0,02	0,005	balance		
M1E - Copper (<i>Carl Schreiber GmbH certificate</i>)												
Chemical element	Ag	Ni	Fe	Sb	As	Zn	S	O	Cu			
wt.%	0,012	0,003	0,002	0,002	0,0017	0,0017	0,005	0,03	balance			
304 L steel (<i>Arcelor Mittal certificate</i>)												
Chemical element	C	Mn	P	S	Si	Cu	Ni	Cr	Mo	N	Co	Fe
wt.%	0,027	1,940	0,0360	0,007	0,523	0,570	9,037	18,730	0,538	0,0864	0,129	balance

To analyze the crystal structure and phase distribution high energy X-ray diffraction (XRD) measurements were carried out using the HZG beamline (P07B) located at PETRA III (electro-storage ring operating at energy 6 GeV with beam current 100 mA) at DESY, Hamburg, Germany. The high energy of synchrotron radiation (87.1 keV, $\lambda = 0.142342 \text{ \AA}$) allowed phase analysis in transmission geometry. The polished samples of dimensions $10 \text{ mm} \times 4 \text{ mm} \times 4 \text{ mm}$ (length/height/width) were ‘scanned’ using so-called continues mode [31], with a step size of 0.2 mm (along the interface). Since the beam size was limited to $0.5 \text{ mm} \times 0.5 \text{ mm}$ the diffraction information from representative large sample volumes (beam size of $0.5 \text{ mm} \times 0.5 \text{ mm} \times 4 \text{ mm}$) was obtained. The detector was located at a distance of 1321 mm from the sample.

Specimens for structural analyses were extracted from the clads in the as-welded state, perpendicular to the transverse direction (TD). This means that the sample edges were parallel to the normal (ND) and the detonation (DD) directions¹. SEM analyses were carried out with the use of an FEI Quanta 3D equipped with a backscattered electrons (BSE) and secondary electrons (SE) detectors. The chemical composition of the reaction products was determined using energy dispersive X-ray spectrometry (EDS). For detailed microstructure investigations, thin foils were cut-off from the clad perpendicular to the TD using a FEI Quanta Focus Ion Beam (FIB) device. The distribution of elements in the solidified melt regions was carried out employing FEI Technai Super TWIN G² FEG TEM equipped with a high-angle annular dark-field scanning/transmission detector (HAADF/STEM) and EDS microanalysis system. To estimate the changes in the hardening across the weld interface Vickers microhardness measurements were performed in the DD/ND section. The tests were carried out with a load of 50 G and a dwell time of 15 s on a finely polished section. The obtained microhardness values were the average of three indentations. The microhardness of the materials before cladding was 234 HV, 84 HV, and 150 HV for SS, Cu, and Ta, respectively. The sheets in the initial states were characterized by uniform and fully recrystallized structures.

3. Results

The macro-scale analyses *via* visual inspection and low magnification SEM/BSE imaging confirmed the high quality of the Ta/Cu/SS and Ta/SS clads, without visible sheets delamination, voids and cracks (Figs. 2 and 3a).

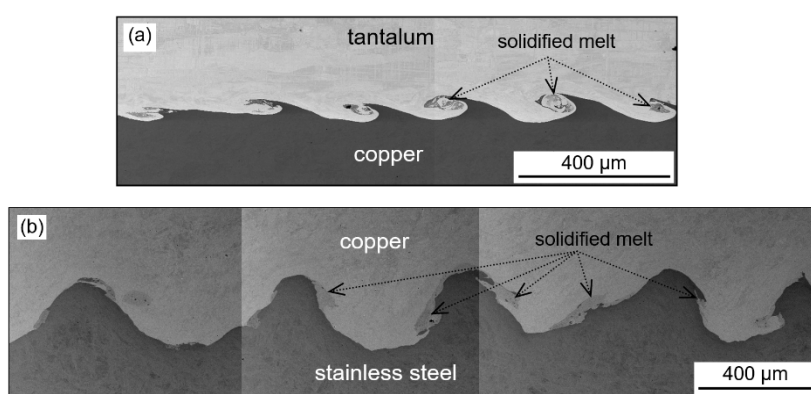


Fig. 2. SEM/BSE images showing a wavy morphology of the interfaces with the melted regions situated: (a) in the wave vortices (case of the Ta/Cu interface), (b) at the crests of the wave (case of the Cu/SS interface).

¹ In the central part of clad the rolling direction (RD) of initial sheets/plates is parallel to the DD.

All the interfaces show regular wavy structures, however, with different wave parameters. In the case of Ta/Cu/SS clad the top interface (Fig. 2a), i.e. between the flyer and interlayer sheets (Ta/Cu), was characterized by significantly smaller amplitude and period than the bottom one, i.e. between Cu interlayer and SS base plate (Fig. 2b). In the case of Ta/SS clad the interface is quite similar to that observed for the Ta/Cu one, with relatively small wave parameters (Fig. 3a).

The wave formation coincides with the occurrence of melted regions, which are preferentially situated at the wave crest and in the vortex core. These reaction regions may exhibit a different form: large, nearly equiaxed zones are mostly situated inside the wave vortexes, thick layers of the solidified melt are situated on the crest of the wave, whereas extremely thin layers in the wave valley. Large melted regions located in the wave vortexes can be completely surrounded by Ta (Fig. 3b) without any contact with the steel plate or can be partly adjacent to the steel plate, as shown in Fig. 3c.

3.1. Microstructure and chemical composition of the melted regions at tantalum to stainless steel interface

SEM/BSE images show high sensitivity to differences in atomic number between solidified melt regions and parent metallic sheets, suggesting significant chemical composition changes across the interfaces.

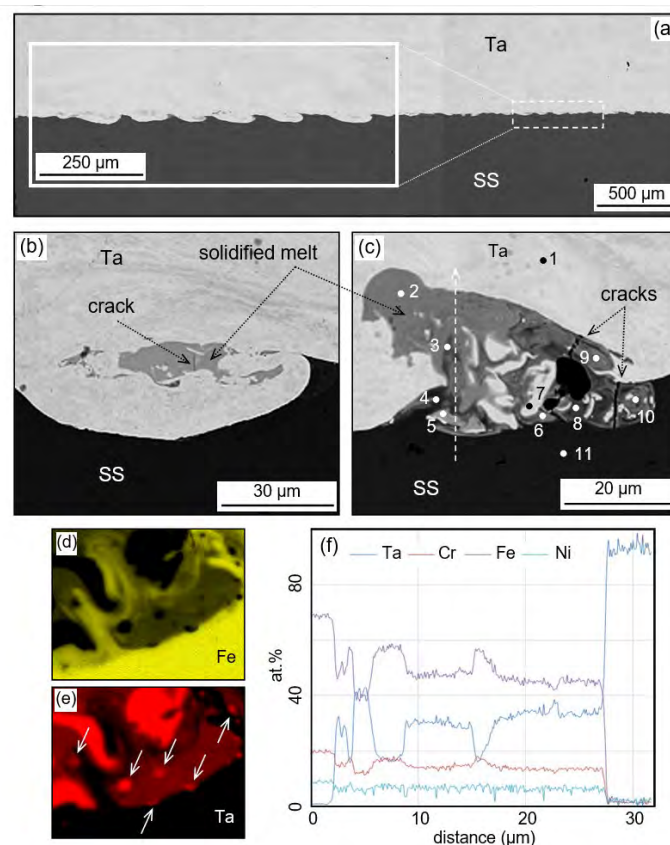


Fig. 3. (a) Interface between Ta and stainless steel (in the centre of the clad) taken in the longitudinal section. Microstructure of the interfacial region showing solidified melt region: (b) completely enclosed inside Ta and (c) being partly in contact with SS. (d, e) Typical distribution of Fe and Ta in the reaction zone showing Ta particles inside the solidified melt. (f) SEM/EDS chemical composition measurements along line scan marked in (c) by a dashed arrow. White arrows in (e) indicate small Ta particles in the solidified melt.

The internal microstructure of the melted regions locked inside the tantalum layer exhibits alternating BSE contrast being evidence for strong chemical composition changes. This is confirmed by SEM/EDS chemical composition mapping of Ta and Fe which reveals a rotational character of the distribution of the elements (Figs. 3d, e). The concentration of main elements varies significantly which can be seen in SEM/BSE images (Fig. 3c and Table 2). Based on the SEM/EDS line scan measurements the concentration of main elements ranges between: $\text{Fe}_{(0.20-0.55)}\text{Cr}_{(0.10-0.18)}\text{Ni}_{(0.03-0.09)}\text{Ta}_{(0.20-0.70)}$ (Fig. 3f).

Table 2. Chemical composition of melted region between tantalum and stainless steel sheets. The points are marked in Fig. 3c

Point no.	Chemical element content (at.%)			
	Cr(K)	Fe(K)	Ni(K)	Ta(L)
1	0,0	0,0	0,0	100,0
2	13,8	48,2	6,1	31,9
3	17,6	59,4	7,1	15,9
4	18,9	68,1	8,1	4,9
5	12,0	42,1	5,2	40,7
6	1,0	4,0	0,3	94,7
7	14,8	50,8	6,4	28,1
8	18,1	62,7	7,6	11,7
9	15,0	52,3	6,5	26,2
10	15,6	55,0	7,0	22,4
11	19,3	71,7	9,0	0,0

Closer examination shows other noteworthy details of the non-homogeneous distribution of main elements in solidified melt regions. The TEM thin foil that was extracted from an area near the interface, as presented in Fig. 4, shows that the solidified melt region enclosed within the tantalum is composed of mixed amorphous and nano-grained phases (very often in the form of small dendrites). The chemical composition of a given area strongly depends on the location within the region. For the case presented in Fig. 4 chemical composition of the melted region was determined to be as follows: $\text{Fe}_{(0.6-0.7)}\text{Cr}_{(0.17-0.21)}\text{Ni}_{(0.07-0.1)}\text{Ta}_{(0.04-0.15)}$.

In the case of a very thin layer of solidified melt, the structural and chemical composition changes can be directly related to the distance from the parent sheets/plates. As an example, a continuous reaction layer with a thickness of 0.5 – 1.0 μm is presented in Figs. 5a, b. The SAED patterns confirmed the presence of sublayers that have a crystalline, mixed ultra-fine-grained/amorphous or amorphous character (starting from the stainless steel plate). The TEM/EDS point measurements inside the particular sublayers show a gradual enrichment of Ta and depletion of Fe, Cr, and Ni as the tantalum sheet approaches. An amorphous and ultra-fine-grained sublayer of an average chemical composition close to ('1') - $\text{Ta}_{0.31}\text{Fe}_{0.48}\text{Cr}_{0.14}\text{Ni}_{0.07}$ is adhering to the tantalum sheet (Fig. 5b). As the stainless steel plate approaches the ultra-fine-grained/amorphous sublayer is gradually substituted with a thin sublayer composed of fine and

then coarser crystallites (or dendrites) of chemical composition close to ('2') - $Ta_{0.19}Fe_{0.54}Cr_{0.16}Ni_{0.11}$. Finally, near the stainless steel plate, a sublayer composed of small elongated grains of a chemical composition close to ('3') - $Ta_{0.11}Fe_{0.60}Cr_{0.17}Ni_{0.12}$ is detected. The distribution of different elements across the interface, shown in Figs. 5c-f, indicate that inside the continuous reaction region the sublayers of the solidified melt situated closer to the stainless steel plate are enriched with Fe, Cr and Ni. Consequently, the concentration of tantalum near the tantalum sheet is the highest and then it successively decreases as the distance from the Ta sheet increases.

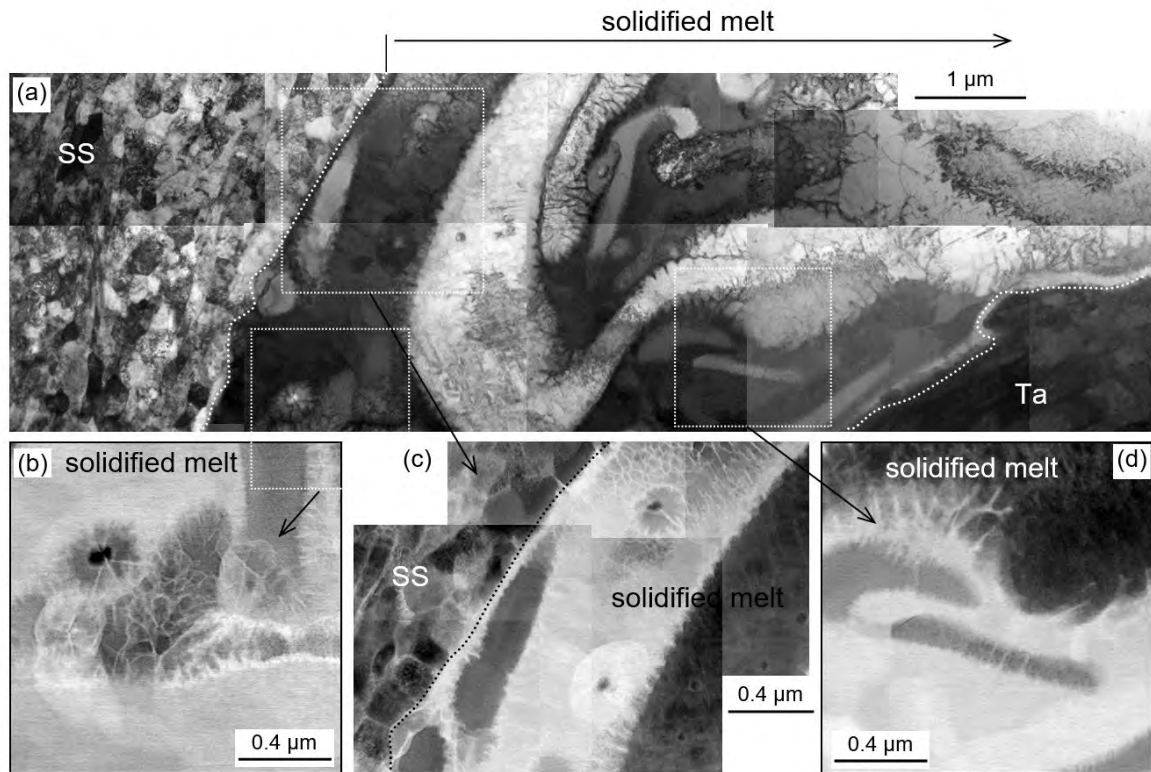


Fig. 4. (a) TEM bright field image showing the internal microstructure of solidified melt region near the Ta/SS interface. (b-d) STEM/HAADF images presenting details of the microstructure of solidified melt in different areas of the reaction region: (b) dendrites, (c) dendrites and parts of stainless steel 'plunged' in Ta, (d) Ta 'diffusion channels' in the stainless steel.

3.2. Microstructure and chemical composition of the melted regions at the interfaces of the Ta/SS clad with copper interlayer

Both interfaces in the tri-layered Ta/Cu/SS clad show regular wavy structures. However, the wave parameters are different, when the base plate/interlayer interface and the flyer/interlayer interface (Fig. 2) are compared. It is noteworthy that for this clad the bottom wavy structure between the copper sheet and stainless steel plate was characterized by significantly larger wave parameters than the upper one, i.e. between tantalum and copper. At the tantalum/copper interface, the melted regions are formed mostly inside the wave vortexes, whereas in the case of copper to stainless steel interface on the crests of the wave.

3.2.1. Solidified melt regions at the Ta/Cu interface

The microstructure of melted regions between tantalum and copper sheets at first approximation can be described as a mixture of Cu and Ta particles of different sizes. Figure 6 shows

SEM/BSE micrographs with a typical structure of the reaction region composed of tantalum spherical particles and dendrites distributed in the copper matrix. The size of spherical particles of tantalum falls typically within the range from 50 nm to 500 nm. Nevertheless, the micro-volumes in which the matrix material was Ta and Cu was in the form of compact spherical aggregates were also experimentally found, as presented in [15]. Therefore, the ‘average’ chemical composition inside the reaction region (detected by SEM/EDS system) may vary from 0% to 100% of a given element. No metastable phases were detected in this work. But, as has been shown by Parchuri et al. [14], the spherical particles and dendrites composed of pure Ta or Cu may coexist with decagonal quasicrystals or Ta_xCu_{1-x} intermetallic phases.

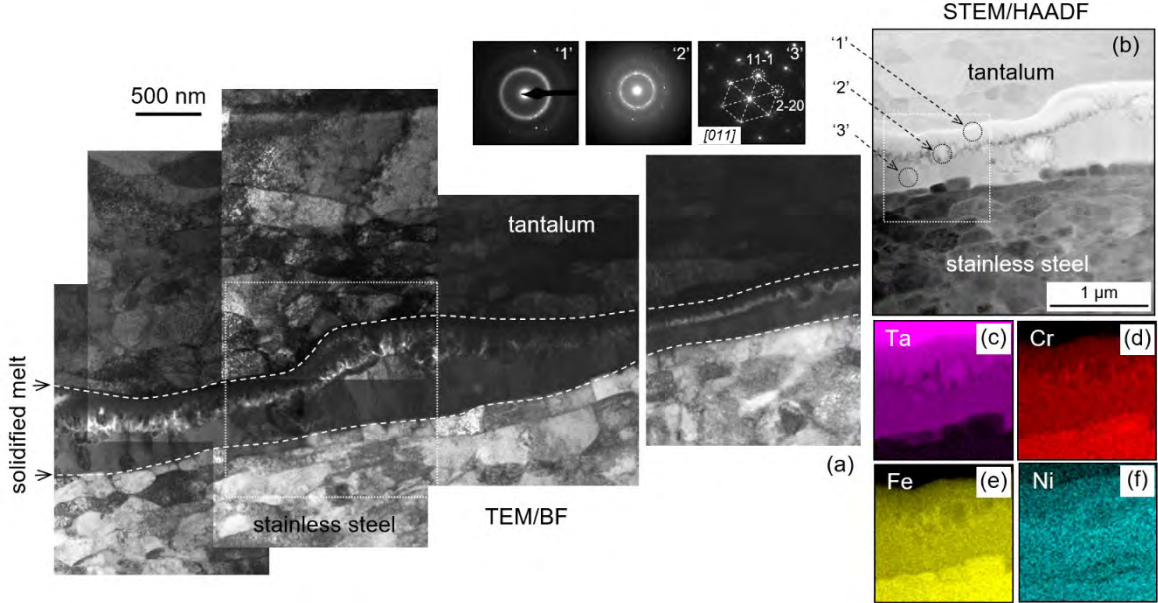


Fig. 5. (a) TEM/BF microstructure near the Ta/SS interface showing the thin continuous reaction layer. (b) STEM/HAADF image from the area marked in (a) by dotted box, with (c-e) the TEM/EDS maps showing the distribution of: Ta, Fe, Cr, and Ni.

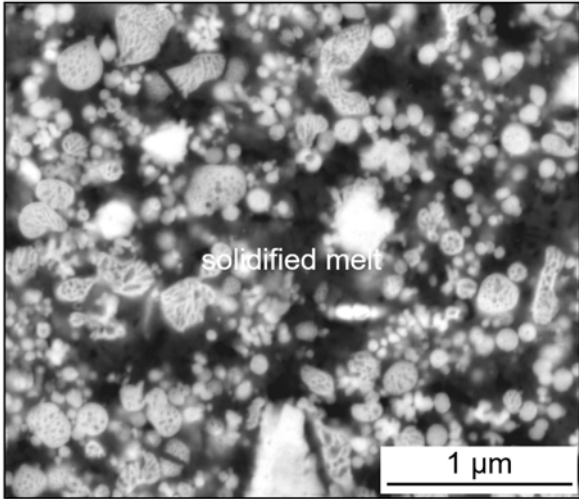


Fig. 6. SEM/BSE image presenting the microstructure of melted region between Ta and Cu sheet.

Due to the small thickness of the phases involved a more accurate characterization of solidified melt region was obtained using TEM. Figure 7 reveals the TEM microstructure of the reaction region using STEM/HAADF imaging. For the most part, this region was composed of dendrites

mixed with spherical particles. The structure composed of Ta dendrites dispersed in the Cu matrix is similar to that received after arc melting of tantalum and copper electrodes during Ta-Cu composite formation [33], whereas a mixture of spherical particles and dendrites was observed in a similar Cu-Nb system (also showing no mutual solubility) [34]. The TEM/EDS chemical composition maps (Fig. 8) confirm that the solidified melt region is exclusively composed of pure Ta and Cu.

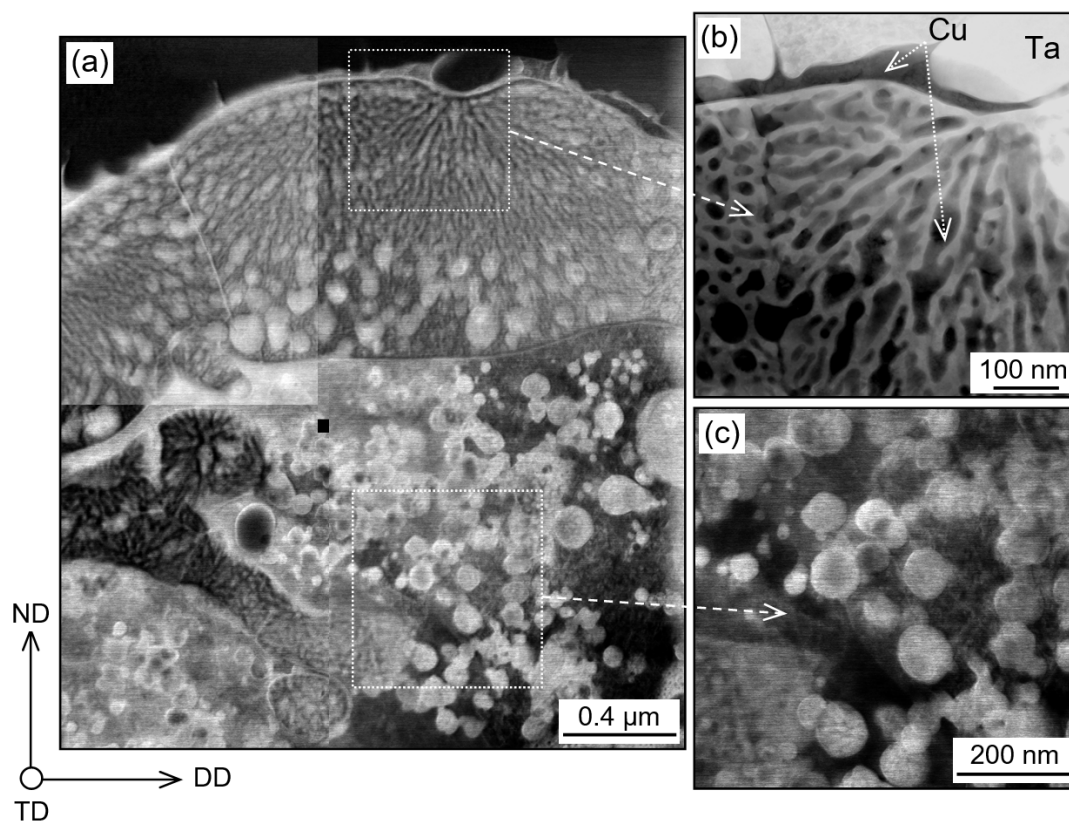


Fig. 7. Microstructure of the reaction region between Ta/Cu interface from the Ta/Cu/SS clad presenting various morphologies of solidified melt. (a) General view of the microstructure of solidified melt near the Ta sheet. (b) Ta dendrites filled with Cu, (c) spherical particles of tantalum in the copper matrix. (a, c) TEM/BF and (b) HAADF/STEM imaging.

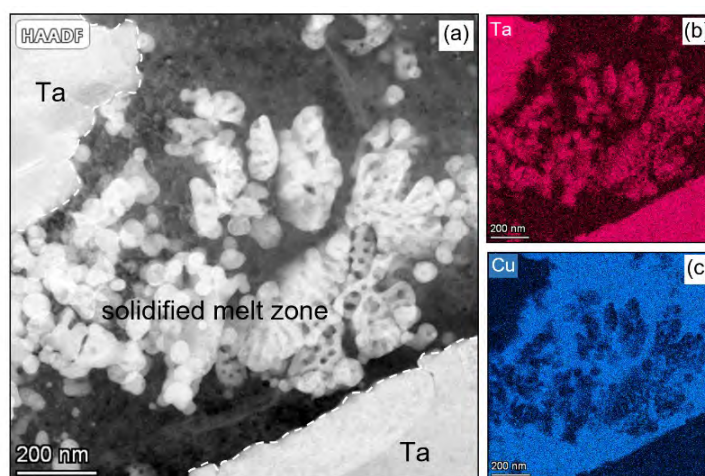


Fig. 8. (a) STEM/HAADF image of a microstructure of the melted region between tantalum and copper from Ta/Cu/SS clad. (b, c) TEM/EDS chemical composition maps showing the distribution of (b) Ta and (c) Cu.

3.2.2. Solidified melt regions at the SS/Cu interface

Figures 9a and b show SEM/BSE micrographs with typical microstructures of the reaction region between copper interlayer and stainless steel plate. The melted regions are composed of fine-grained phases (Fig. 9c) with the concentration of main elements in the range between $\text{Cu}_{(0.09-0.43)}\text{Fe}_{(0.35-0.68)}\text{Cr}_{(0.10-0.19)}\text{Ni}_{(0.02-0.08)}$.

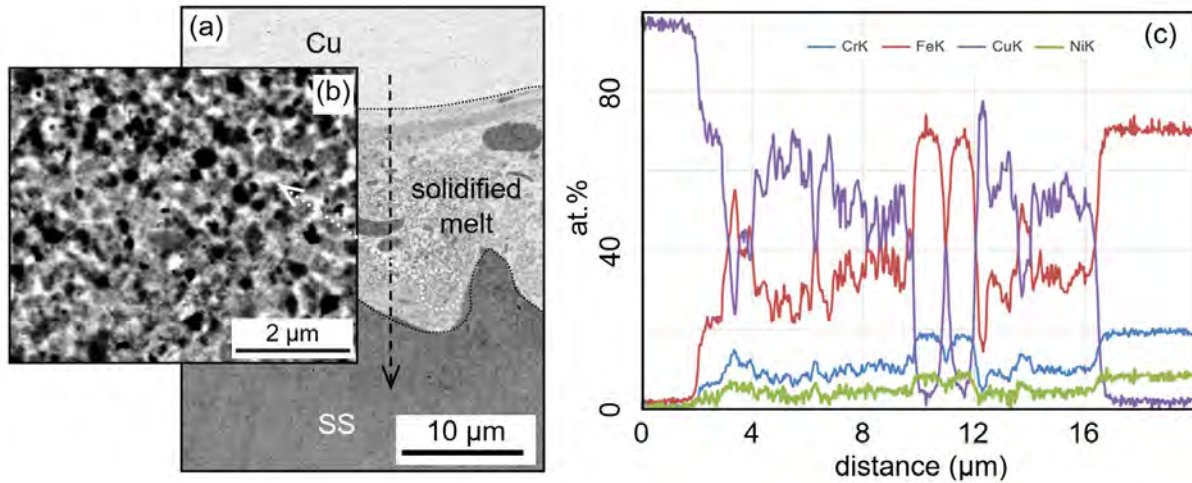


Fig. 9. (a) SEM/BSE image presenting microstructure of the interfacial layer near the copper and stainless steel sheets. (b) Internal microstructure of reaction region, and corresponding (c) SEM/EDS line scan showing chemical composition changes in the solidified melt region (along black dashed arrow marked in (a)).

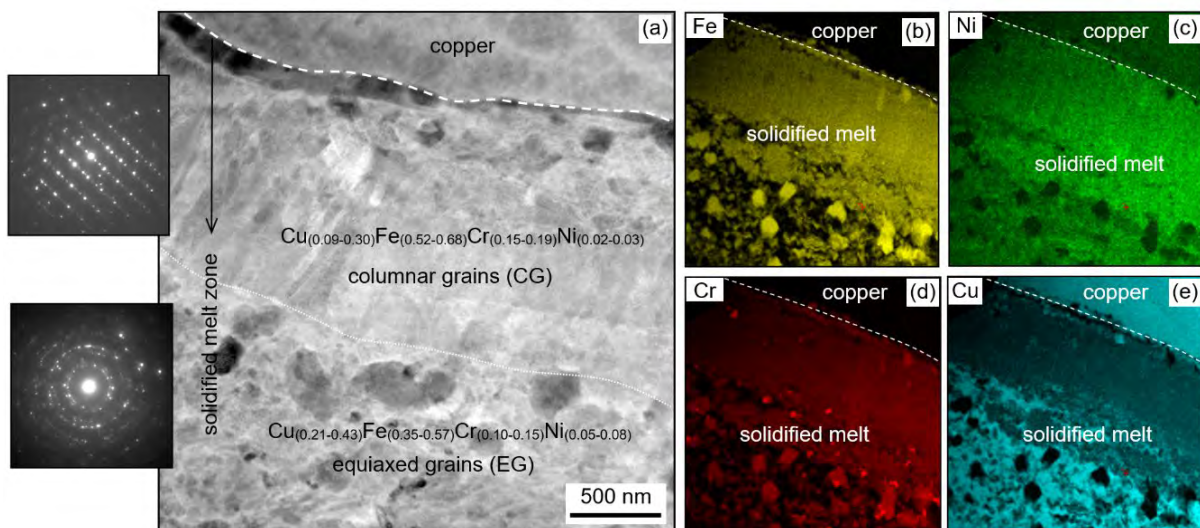


Fig. 10. (a) STEM/HAADF image of microstructure of solidified melt region between copper and stainless steel near the copper/solidified melt boundary and corresponding given areas selected area diffraction patterns. (b-e) STEM/EDS maps showing the distribution of main elements.

Figure 10 shows the microstructure near the Cu/SS interface observed at TEM scale. The grains that nucleate inside the melted region near the copper sheet form a sublayer composed of small elongated grains with longer axis almost perpendicular to the interface between copper and

reaction region. This indicates a very efficient heat transfer from the molten volume towards the copper sheet. In the central part of the solidified melt region only equiaxed, ultra-fine grains (or small dendrites) are formed. At the SS/solidified melt boundary, only fine, nearly equiaxed grains are formed. Despite various chemical compositions identified inside solidified melt regions, to a larger extent the phases are enriched in Cu (ranging between 60% and 90%).

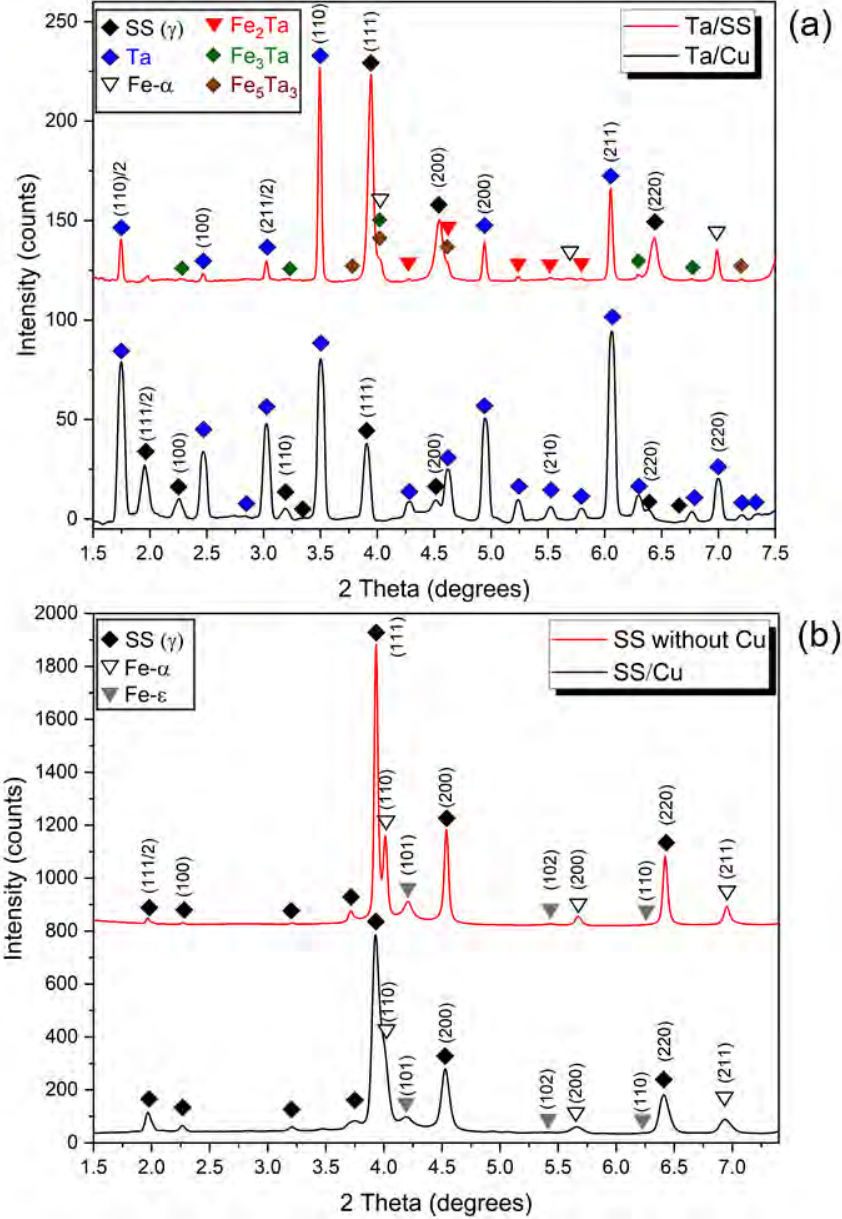


Fig. 11. X-ray synchrotron diffraction patterns for the Ta/Cu/SS and Ta/SS metal compositions taken from the area: (a) including the interfacial layers of neighbouring sheets/plates ($0.5 \times 0.5 \times 10 \text{ mm}^3$), (b) only SS parts for the next nearest region to the interfaces.

Another common feature observed in solidified melt region close to the copper and stainless steel sheets/plates is the presence of Fe-Cr- and Cr-rich precipitations (Figs. 10b-e). The chromium-rich volumes that form during the solidification process of the melted regions, lead to depleting of the surrounding matrix, where the Cr content may drop below the critical concentration. This can weaken the joint by reducing the corrosion resistance of the solidified

melt [35]. It is, therefore, necessary to apply a high-temperature heat treatment to dissolve Fe and/or Cr rich precipitates by diffusion in the solid state².

3.3. Phase identification using X-ray synchrotron radiation

In order to identify the phase composition and crystallographic structure of the phases appearing in the solidified melt regions synchrotron X-ray diffraction was performed. Figure 11a shows a diffraction spectrum (intensity vs. 2θ angle) for the Ta/Cu and Ta/SS interfaces. Diffraction pattern taken at the Ta/Cu interface (from Ta/Cu/SS composite) indicates only reflections coming from pure Ta and Cu. No other (intermetallic) phases have been identified in the reaction region. Surprisingly, high intensities of half-order Bragg peaks are determined. It appears to account for a certain fraction of the dissolved atoms which translates into double-fold periodicity in real space. In the case of Ta/SS interface the reflections corresponding to γ -Fe, α -Fe and Ta are dominant. However, a closer look reveals also the presence of reflections coming from the equilibrium phases, i.e. Fe₂Ta, Fe₅Ta₃, and Fe₃Ta.

Additionally, areas in the layer of steel in close proximity to the interface were investigated (Fig. 11b). The obtained diffraction patterns mainly show reflections originating from the γ -Fe phase, however, accompanied by a high 'portion' of ε -Fe and α -Fe phases. In principle, the occurrence of α -Fe can be linked with two processes. The first one is associated with martensitic transformation while the other one with the decomposition of austenite. Both effects were observed microscopically, i.e. regions with pure Fe composition and martensitic platelets. Another issue is the formation of ε -Fe phase. Following the phase-temperature state diagram for pure Fe [13, 37] the presence of ε -Fe phase can be attributed to very high pressure, which can stimulate the $\gamma \leftrightarrow \varepsilon$ and $\alpha \leftrightarrow \varepsilon$ phase transformations. During EXW the pressure of the material drops down almost instantaneously, while the cooling process lasts much longer [6]. However, both factors (pressure and temperature) cause that the layers in the close proximity to the interface can undergo a series of remarkable phase transformations, as discussed in detail by Bataev et al. [13]. The $\gamma \rightarrow \varepsilon$ transformation can occur only under large stresses. The stresses lead to the formation of a large number of structural defects in the deformed austenite (dislocations and stacking faults), this would, in turn, facilitate hexagonal ε -Fe phase nucleation [37-39]. A similar mechanism of deformation has been reported to occur in [40, 41].

Another factor that makes the $\gamma \rightarrow \varepsilon$ transformation easier is the compressive nature of the process. Generally, a much lower amount of ε -Fe phase is formed under tension loading, while using compression the ε -martensite is much more readily formed [41, 42]. As the observed volume fraction of ε -Fe phase is relatively large, it corresponds quite-well with a compression force created by the explosion. However, it should be noted, that the given interpretation of ε -Fe phase formation in steel should be carried out with great caution due to high dynamics of the EXW process.

3.4. Microhardness of solidified melt

In order to correlate the microstructure of solidified melt with the strength properties of the clads the microhardness measurements were performed. The microhardness of the reaction region at Ta/Cu interfaces reached values between 200 and 270 HV (Fig. 12), whereas the microhardness measured in the solidified melt region situated between the copper sheet and

² The selected area diffraction analysis (in areas enriched with Fe and/or Cr) together with the analysis related to the carbon distribution do not show formation of carbides of FeCrC or FeC-types.

stainless steel plate amounts to 215-370 HV. These values significantly differ from those obtained for tantalum to stainless steel clads, where the microhardness of intermetallic phases is ranged between 720 and 1080 HV. This is 2 - 3 times as much as in strain-hardened layers of stainless steel sheet, independently on analysed clad.

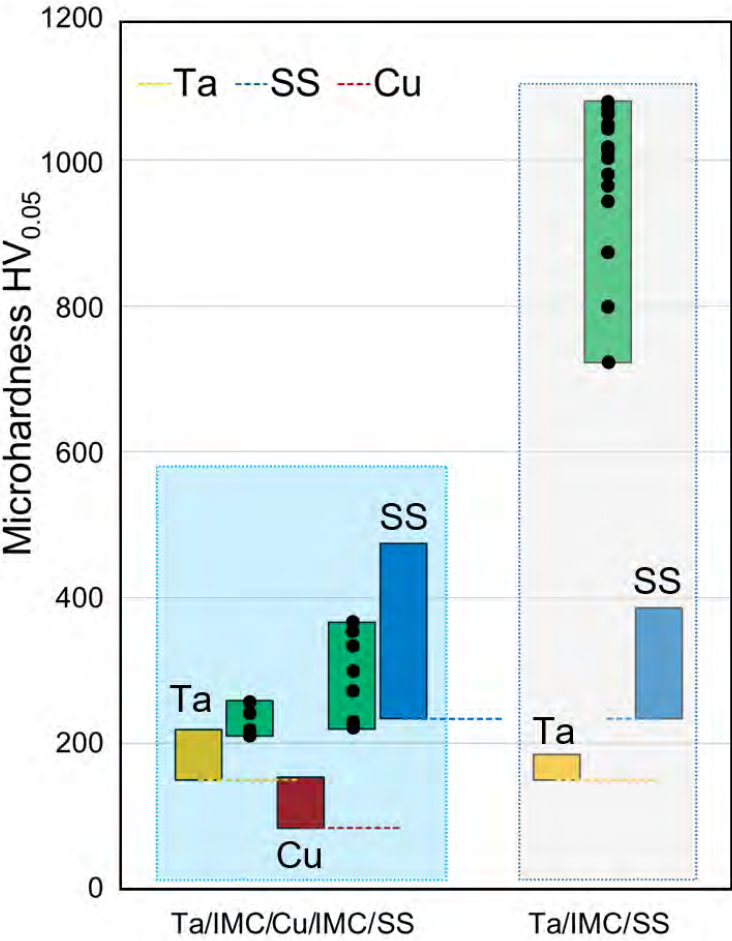


Fig. 12. Variation of microhardness values in the layers near the interface of Ta/SS and Ta/Cu/SS metals compositions. Green boxes indicate the range of the microhardness values measured inside the reaction regions (formed between particular metal sheets). Black circles inside green boxes mark the values of particular microhardness measurements inside solidified melt, whereas dashed horizontal lines the microhardness of parent sheets in fully recrystallized states.

4. Discussion

The evolution of the microstructure in certain micro-volumes of melted region and its influence on properties of the Ta/Cu/SS and Ta/SS clads were studied at different scale levels. Particular attention was paid to the phase composition of solidified melt, where the most spectacular transformations take place due to dramatic temperature changes. The calculations made by Bataev et al. [6] show that the heating rate during the temperature increase period can exceed 10^9 K s^{-1} . As the process is extremely fast, there is no time for the heat to be transferred away from the melted region, and any additional increase in temperature leads to local melting. In the second period, the thermodynamic conditions are very similar to that observed during spin melting since the melted volumes are subjected to extremely high cooling rates which always exceed $10^5\text{-}10^7 \text{ K s}^{-1}$, e.g. [6, 12]. One of the most important questions is – what is the maximum

temperature that can be reached during EXW? This applies especially to Ta-based composites since the melting point of Ta is extremely high.

4.1. The evolution of microstructure near Ta/Cu and Cu/SS interfaces during rapid cooling

In earlier works [28, 43] the authors have argued that the reaction region between EXW tantalum and copper sheets exhibits a mechanical mixture of the dispersed Ta and Cu particles. The approach proposed in [43] is based on the assumption that during dynamic interaction of copper and tantalum sheets along collision line, a cumulative jet consisting of liquid copper (lower melting point) moves directly on the surface of the tantalum sheet and interacts with the roughness of the latter. In this mechanism, there is no need to exceed the melting point of tantalum since the particles of tantalum are plunged into copper. However, it is very difficult to state without any doubt whether this mechanism is the only one, just dominant or whether another mechanism plays a key role in 'shaping' the structure of the solidified melt. This results from the fact that in many cases (as it was also observed in this work) the structure of the reaction region is composed of Cu spherical particles plunged into Ta matrix [15]. Moreover, the occasional formation of non-equilibrium intermetallic phases cannot be excluded due to high pressure and extremely rapid cooling. In EXW clads the decagonal quasicrystals of metastable phases were documented by Parchuri et al. [14]. In thin films, where the solidification terms are very similar to those observed during EXW, the Ta_xCu_{1-x} metastable phases of different morphology were found to coexist along with pure tantalum and copper particles. For instance, a substitutional solid solution was observed by Cullis et al. [44], amorphous phases were identified by Nastasi et al. [45] and Gong et al. [46], whereas nano-grained phases by Purja Pun et al. [47] and Rajagopalan et al. [48].

Therefore, another explanation of structural changes inside the melted regions between Ta-Cu and Fe-Cu sheets can be proposed. It is based on the solidification of the liquids showing miscibility gap. For such systems, Munitz and Abbaschian [49] and Mondolfo [50] argued that under cooling rates of the order of $10^5 - 10^6$ K/s, a supercooled liquid may continue to supercool further. Based on the results obtained for a similar Nb-Cu system (also showing miscibility gap) various situations can be considered due to the dynamics of supercooling, which plays a central role in the final morphology of solidified melt [51]. For alloys that entered the miscibility gap prior to nucleation, the entire cross-section will consist of spherical elements. When alloy is quenched from the solid and liquid region the melt separation will occur within the dendrites. Since there is a lack of mutual solubility of tantalum and copper in the whole range of temperatures, the final structure is predominantly composed of particles/dendrites of pure tantalum and copper.

The microstructure of solidified melt region between Cu and steels is qualitatively different. However, their formation can be explained based on similar assumptions associated with miscibility gap existence. Since the mutual solubility of Cu in Fe at higher temperatures is considerable, i.e. ~13 wt.% of Cu in γ -Fe at 1673 K, and 1.9 wt.% of Cu in α -Fe at 1123 K, therefore, after rapid cooling, final microstructures are composed of fine-grained phases (or small dendrites) of various chemical composition. Currioto et al. [52] show that under rapid cooling the supercooling of liquids below a certain temperature resulted in melt separation into a Fe-rich (L_1) and a Cu-rich (L_2) liquids. Depending on the contents of both elements, the grains/dendrites with depleted Fe solidify from the L_1 , whereas those enriched with Fe, solidify from the L_2 . This is one of the reasons which can explain the formation of phases of various chemical composition.

The above clearly indicates that the decisive role in formation of solidified melt morphologies is played by local melting of joined materials (including Ta), and mechanical mixing can only

play a supporting role (if at all). However, many aspects of solidified melt formation, such as liquid phase separation, nucleation during solidification and microstructure evolution due to a significant increase of mutual solubility of Cu and Fe (especially in γ -Fe) at high temperatures and eutectoid transformation, etc., are not yet fully understood and further studies are needed.

In an effort to shed more light on the issue of the morphology of solidified melt and changes near the interface layers of parent sheets/plates synchrotron measurements were performed. As it was shown the Cu layer significantly reduces the formation of brittle intermetallic phases. This applies both to the areas close to Ta/Cu and to Cu/SS interface. No intermetallic phases have been detected in the reaction regions. On the other hand, the high intensities of half-order peaks indicate a certain fraction of the dissolved atoms which permits a higher alloying level even in the systems which are practically insoluble over a wide temperature range. Thus, severe deformation and extremely high pressure during EXW may increase the solid solubility level enabling formation of metastable phases in parent sheets/plates. Furthermore, it was found that the use of Cu intermediate layer reduces the amount of α -Fe and ϵ -Fe phases in stainless steel. The observed volume fraction of α -Fe and ϵ -Fe phases is lower for Ta/Cu/SS than for Ta/SS clad and it amounts to 12.5% and 18.2% for α -Fe, and 5.2% and 3.8% for ϵ -Fe phases. Most likely it is due to the Cu intermediate sheet which is able to accommodate a large part of plastic deformation.

4.2. *Microstructure vs. strength properties*

A relatively low microhardness was measured in the reaction regions at the Cu/SS and Ta/Cu interfaces as compared to Ta/SS interface and strain-hardened layers of stainless steel plate. Despite the strain-hardened layers of parent sheets exhibit high hardness, the recovered and/or recrystallized structure near the interface and easy cracks nucleation inside the melted regions can countervail the overall strengthening effect. The presence of brittle amorphous and ultra-fine-grained phases inside the solidified melt regions near the Ta/SS interface improves the clad strength but also decreases the ability for clad shaping. Moreover, the micro-/macro- cracks that appear intensively inside the melted regions during the liquid solidification decrease the overall-clad strength. During further clad shaping the micro-/macro-cracks can propagate towards parent materials. At the Cu/Ta and Cu/SS interfaces, the microhardness of solidified melt regions is lower than the one in strain-hardened layers of stainless steel plate. It is clear that the solidified melt regions shall not cause an increase in clad strength. On the other hand, the cracks in these relatively soft reaction regions are observed only accidentally and, therefore, this factor cannot be regarded as affecting the clad strength.

5. Summary

The present study describes the morphology and microhardness of the solidified melt regions at the Ta/Cu, Ta/SS and Cu/SS interfaces of EXW tantalum to stainless steel clads with and without copper interlayer. The following detailed conclusions can be drawn:

- Multiscale analyses revealed a complex and hierarchical microstructure of interfacial layers. Macro-scale observations showed the formation of wavy joints with reaction regions situated inside and at the crest of the wave vortexes. The occurrence of a liquid phase at the interfaces is the most important feature leading to the formation of the reaction regions that are always well-defined by sharp BSE contrast due to sharp chemical composition changes.
- Micro-/nano- scale analyses revealed an internal microstructure of the reaction regions. The formation of non-equilibrium phases of various chemical compositions, with some

quantity of cracks, is the most characteristic feature of the internal structure of large solidified melt regions formed near the Ta/SS interface. Three brittle intermetallic compounds, such as Fe₂Ta, Fe₅Ta₃, and Fe₃Ta were also detected. The thin layer of the solidified melt is always composed of several sublayers, which reveal amorphous, fine- and coarse-grained structures of alternating chemical composition. The solidified melt regions near the Ta/Cu interface consist of a mixture of pure copper and tantalum particles or dendrites, whereas near the Cu/SS interface are composed of phases based on elements of both neighboring sheets. The reaction regions near the Ta/Cu and Cu/SS interfaces are almost free of discontinuities.

- The structural changes in the reaction region between Ta-Cu and Fe-Cu sheets can be explained based on the mechanism of solidification of the systems exhibiting miscibility gap. In these systems, the dynamics of super-cooling plays a central role in the final microstructures of solidified melt, which can consist of spherical elements and/or dendrites.
- The hardness of the reaction region near the Ta/Cu or Cu/SS interfaces is 2 – 3 times lower than those measured near the Ta/SS interface, and it does not exceed the hardness of interfacial (strain-hardened) layers in stainless steel.
- The diffraction patterns obtained in the steel layers in the very close proximity to the interface show mainly reflections originating from the γ -Fe phase, however, accompanied by a high portion of α -Fe and ε -Fe phases. The presence of hexagonal ε -Fe phase can be attributed to severe plastic deformation and extremely high pressure, which can stimulate the $\gamma \leftrightarrow \varepsilon$ and $\alpha \leftrightarrow \varepsilon$ phase transformations. It was found that the use of Cu interlayer reduces the amount of α -Fe and ε -Fe phases in steel.

Acknowledgements

This research was funded by the National Centre for Research and Development of Poland under grant TECHMATSTRATEG2/412341/8/NCBR/2019 (EMuLiReMat). The authors give thanks to Mr. Z. Szulc and High Energy Technologies Works ‘Explomet’ (Opole, Poland) for the provision of the Ta-based clads.

References

1. D. Frey, J. Banker, Recent successes in tantalum clad pressure vessels manufacture: A new generation of tantalum vessels, Proceedings of Corrosion Solutions Conference, USA: Wah Chang 2003, 163-169, Paper no. 22.
2. I.F. Danzig, R.M. Dempsey, A.B. La Conti, Characteristic of tantalided and hafnided samples in high corrosive electrolyte solutions, Corrosion, 27 (1971) 55-62. <https://doi.org/10.5006/0010-9312-27.2.55>
3. F. Cardarelli, P. Taxil, A. Savall, Tantalum protective thin coating techniques for the chemical process industry: Molten salts electrocoating as a new alternative, Int. J. of Refractory & Hard Materials, 14 (1996) 365-381. [https://doi.org/10.1016/S0263-4368\(96\)00034-0](https://doi.org/10.1016/S0263-4368(96)00034-0).
4. T.Z. Blazynski, Explosive Welding, Forming and Compaction, Applied Science Publishers LTD, New York (1983). <https://doi.org/10.1007/978-94-011-9751-9>.
5. B. Crossland, J.D. Williams, Explosive welding, Metall. Rev., 15(1) (1970) 79-100 <https://doi.org/10.1179/mtlr.1970.15.1.79>

6. I.A. Bataev, D.V. Lazurenko, S. Tanaka, K. Hokamoto, A.A. Bataev, Y. Guo, A.M. Jorge Jr., High cooling rates and metastable phases at the interfaces of explosively welded materials, *Acta Mater.*, 135 (2017) 277-289. <https://doi.org/10.1016/j.actamat.2017.06.038>
7. H. Paul, M.M. Miszczyk, R. Chulist, M. Prażmowski, J. Morgiel, A. Gałka, M. Faryna, F. Brisset, Microstructure and phase constitution in the bonding zone of explosively welded tantalum and stainless steel sheets, *Mat. Design*, 153 (2018) 177-189. <https://doi.org/10.1016/j.matdes.2018.05.014>.
8. M. Yang, H. Ma, Z. Shen, Z. Huang, Q. Tian, J. Tian, Dissimilar material welding of tantalum foil and Q235 steel plate using improved explosive welding technique, *Mater. Design*, 186 (2020) 108348. <https://doi.org/10.1016/j.matdes.2019.108348>.
9. J. Song, A. Kostka, M. Veehmayer, D. Raabe, Hierarchical microstructure of explosive joints: example of titanium to steel cladding, *Mat. Sci. Engn. A528* (2011) 2641-2647. <https://doi.org/10.1016/j.msea.2010.11.092>
10. I.A. Bataev, A.A. Bataev, V.I. Mali, D.V. Pavliukova, Structural and mechanical properties of metallic-intermetallic laminate composites produced by explosive welding and annealing, *Materials and Design*, 35 (2012) 225-234. <https://doi.org/10.1016/j.matdes.2011.09.030>
11. H. Paul, L. Lityńska-Dobrzyńska, M. Prażmowski, Microstructure and phase constitution near the interface of explosively welded aluminium/copper plates, *Metall. Mater. Trans. A*, 44A (2013) 3836-3851. <https://doi.org/10.1007/s11661-013-1703-1>
12. H. Paul, J. Morgiel, M. Faryna, M. Prażmowski, M. Miszczyk, Microstructure and interfacial reactions in the bonding zone of explosively welded Zr700 and carbon steel plates, *Int. J. Mater Res.*, 106 (7) (2015) 782-792. <https://doi.org/10.3139/146.111230>
13. I.A. Bataev, S. Tanaka, Q. Zhou, D.V. Lazurenko, A.M. Jorge Junior, A.A. Bataev, K. Hokamoto, A. Mori, P. Chen, Towards better understanding of explosive welding by combination of numerical simulation and experimental study, *Mat. Design*, 169 (2019) 107649. <https://doi.org/10.1016/j.matdes.2019.107649>
14. P.K. Parchuri, S. Kotegava, H. Yamamoto, K. Ito, A. Mori, K. Hokamoto, Benefits of intermediate-layer formation at the interface of Nb/Cu and Ta/Cu explosive clads, *Materials Design*, 166 (2019) 107610. <https://doi.org/10.1016/j.matdes.2019.107610>.
15. H. Paul, R. Chulist, I. Mania, Structural properties of interfacial layers in tantalum to stainless steel clad with copper interlayer produced by explosive welding, *Metals*, 10(7) (2020) 969. <https://doi.org/10.3390/met10070969>.
16. V.I. Mali, A.A. Bataev, Iu. N. Maliutina, V.D. Kurguzov, I.A. Bataev, M.A. Esikov, V.S. Lozhkin, Microstructure and mechanical properties of Ti/Ta/Cu/Ni alloy laminate composite materials produced by explosive welding, *Int. J. Adv. Manuf. Technol.*, 93 (2017) 4285-4294. <https://doi.org/10.1007/s00170-017-0887-8>.
17. M.S. Pushkin, B.A. Greenberg, M.A. Ivanov, A.V. Inozemtsev, A.M. Patselov, Y.P. Besshaposhnikov, Microstructure of joints Cu–Ta, Cu–Ti, Cu–Cu, produced by means of explosive welding: fractal description of interface relief, *Composite Interfaces* <https://doi.org/10.1080/09276440.2020.1736880>.
18. Iu.N. Maliutina, A.A. Bataev, I.A. Bataev, K.A. Skorokhod, V.I. Mali, Explosive welding of titanium with stainless steel using bronze - tantalum as interlayer, *Materials of the 9th International Forum on Strategic technology (IFOST), Cox's Bazar, Bangladesh, 21-23 October, 2014*. <https://doi.org/10.1109/IFOST.2014.6991157>.

19. G.P. Bouckaert, H.B. Hix, J. Chelius (1974) Explosive-bonded tantalum-steel vessels. DEHEMA Monograph 76, 9-22
20. P.R. Subramanian, D.E. Laughlin, The Cu-Ta system, Bulletin of Alloy Phase Diagrams, vol. 10/6 (1989) 652-655.
21. L.J. Swartzendruder, Cu-Fe, Phase Diagrams Binary Iron Alloy, ASM International, Ohio, 1990, pp. 1408-1410.
22. S. Currioto, R. Greco, N.H. Pryds, E. Johnson, L. Battezzati, The liquid metastable gap in Cu-based systems, Fluid Phase equilibria, 256 (2007) 132-136
23. V.I. Lysak, S.V. Kuzmin, Explosive welding: Processes and structures, Moscow: Mashinostrenie, 2005 (in Russian).
24. H. Paul, M.M. Miszczyk, A. Gałka, R. Chulist, Z. Szulc, Microstructural and chemical composition changes in the bonding zone of explosively welded sheets, Arch. Metall. Mater., 64 (2) (2019) 683-694. <https://doi.org/10.24425/amm.2019.127599>.
25. H. Zhang, K.X. Jiao, J.L. Zhang, J. Liu, Experimental and numerical investigations of interface characteristics of copper/steel composite prepared by explosive welding, Mater. Design, 154 (2018) 140-152. <https://doi.org/10.1016/j.matdes.2018.05.027>.
26. S. Saravanan, K. Raghukandan, Influence of interlayer in explosive cladding of dissimilar metals, Materials and Manufacturing Processes, 25 (2013) 589-594. <https://doi.org/10.1080/10426914.2012.736665>.
27. H. Paul, Interfacial reactions during explosive bonding, Materials Science Forum, vol. 783-786 (2014) 1476-1481. <https://doi.org/10.4028/www.scientific.net/MSF.783-786.1476>.
28. B.A. Greenberg, M.A. Ivanov, V.V. Rybin, O.A. Elkina, O.V. Antonov, A.M. Patselov, A.V. Inozemtzev, A.V. Plotnikov, A.Yu. Volkova, Yu.P. Bessaposhnikov, The problem of intermixing of metals possessing no mutual solubility upon explosion welding (Cu-Ta, Fe-Ag, Al-Ta), Materials Characterization, 25 (2013) 51-62. <https://doi.org/10.1016/j.matchar.2012.10.011>.
29. A. Durgutlu, B. Güleç, F. Findik, Examination of copper/stainless steel joints formed by explosive welding, Mater. Design, 25 (2005) 497-507. [doi:10.1016/j.matdes.2004.07.021](https://doi.org/10.1016/j.matdes.2004.07.021)
30. H. Zhang, K.X. Jiao, J.L. Zhang, J. Liu, Experimental and numerical investigations of interface characteristics of copper/steel composite prepared by explosive welding, Mater. Design, 154 (2018) 140-152. [doi: 10.1016/j.matdes.2018.05.027](https://doi.org/10.1016/j.matdes.2018.05.027).
31. R. Chulist, L. Straka, H. Seiner, A. Sozinov, N. Schell, T. Tokarski, Branching of {110} twin boundaries in five-layered Ni-Mn-Ga bent single crystals, Materials & Design, 171 (2019) 107703. doi.org/10.1016/j.matdes.2019.107703.
32. H. Paul, R. Chulist, M.M. Miszczyk, M. Prażmowski, Gradient microstructure in the bonding zone of explosively welded sheets, Procedia Manufacturing, 50 (2020) 689-695. <https://doi.org/10.1016/j.promfg.2020.08.124>.
33. US Patent no. 4,600,448, July 15 (1986)
34. A. Munitz, M. Bamberger, A. Venkert, P. Landau, R. Abbaschian, Phase selection in supercooled Cu-Nb alloys, J. Mater. Sci., 44 (2009) 64-73. [doi: 10.1007/s10853-008-3115-y](https://doi.org/10.1007/s10853-008-3115-y).
35. M. Laleh, A.E. Hughes, W. Xu, N. Haghdadi, K. Wang, P. Cizek, I. Gibson, M.Y. Tan, On the unusual intergranular corrosion resistance of 316L stainless steel additively

- manufactured by selective laser melting, *Corrosion Science*, 161 (2019) 108189. <http://dx.doi.org/10.1016/j.corsci.2019.108189>.
36. A.T Dinsdale, SGTE data for pure elements, *Calphad*, 15(4) (2019) 317-425. doi: [10.1016/0364-5916\(91\)90030-N](https://doi.org/10.1016/0364-5916(91)90030-N)
 37. J.W. Brooks, M.H. Loretto, R.E. Smallman, In situ observations of the formation of martensite in stainless steel, *Acta. Metall.* 27 (1979) 1829–1838. [https://doi.org/10.1016/0001-6160\(79\)90073-7](https://doi.org/10.1016/0001-6160(79)90073-7)
 38. T. Suzuki, H. Kojima, K. Suzuki, T. Hashimoto, M. Ichihara, An experimental study of the martensite nucleation and growth in 18/8 stainless steel, *Acta. Metall.* 25 (1977) 1151–1162. [https://doi.org/10.1016/0001-6160\(77\)90202-4](https://doi.org/10.1016/0001-6160(77)90202-4).
 39. A. Das, P.C. Chakraborti, S. Tarafder, H.K.D.H. Bhadeshia, Analysis of deformation induced martensitic transformation in stainless steels, *Mater. Sci. Technol.* 27 (2011) 366–370. doi: [10.1179/026708310X12668415534008](https://doi.org/10.1179/026708310X12668415534008)
 40. V. Tsakiris, D.V. Edmonds, Martensite and deformation twinning in austenitic steels, *Mater. Sci. Eng. A273* (1999) 430–436.
 41. Ł. Rogal, J. Dutkiewicz, Deformation behaviour of high strength X210CrW12 steel after semi-solid processing, *Mater. Sci. Engn. A*, 603 (2014) 93-97. doi: [10.1016/j.msea.2014.01.099](https://doi.org/10.1016/j.msea.2014.01.099)
 42. M. El-Tahawy, P. Jenei, T. Kolonits, G. Han, H. Park, H. Choe, J. Gubicza, Different evolutions of the microstructure, texture, and mechanical performance during tension and compression of 316L stainless steel, *Metal. Mater. Trans. A* 51 (2020) 3437-3460. doi: [10.1007/s11661-020-05782-5](https://doi.org/10.1007/s11661-020-05782-5)
 43. Iu. N. Maliutina, A. A. Bataev, I. A. Bataev, K. A. Skorokhod, V. I. Mali, Explosive welding of titanium with stainless steel using bronze — Tantalum as interlayer, materials of the 9th International Forum on Strategic technology (IFOST), Cox’s Bazar, Bangladesh, 21-23 October, 2014. doi: [10.1109/IFOST.2014.6991157](https://doi.org/10.1109/IFOST.2014.6991157).
 44. A.G. Cullis, J.A. Orders, J.K. Hirvonen, J.M. Poate, Metastable alloy layers produced by implantation of Ag and Ta ions into Cu crystals, *Phil. Mag. B* 37 (1978) 615–630. <https://doi.org/10.1080/01418637808226456>
 45. M. Nastasi, F.W. Saris, L.S. Hung, J.W. Mayer, Stability of amorphous Cu/Ta and Cu/W alloys, *J. Appl. Phys.* 58 (1985) 3052. <https://doi.org/10.1063/1.335855>
 46. H.R. Gong, L.T. Kong, B.X. Liu, Amorphous alloy formation in immiscible Cu-Ta and Cu-W systems by atomistic modelling and ion-beam mixing, *MRS Online Proc. Libr.* 806 (2003)
 47. G.P. Purja Pun, K.A. Darling, L.J. Kecskes, Y. Mishin, Angular-dependent interatomic potential for the Cu – Ta system and its application to structural stability of nano-crystalline alloys, *Acta Mat.* 100 (2015) 377–391. doi: [10.1016/j.actamat.2015.08.052](https://doi.org/10.1016/j.actamat.2015.08.052).
 48. M. Rajagopalan, K. Darling, S. Turnage, R.K. Koju, B. Hornbuckle, Y. Mishin, K. N. Solanki, Microstructural evolution in a nanocrystalline Cu-Ta alloy: a combined in-situ TEM and atomistic study, *Mater. Des.* 113 (2016) 178–185. <http://dx.doi.org/10.1016/j.matdes.2016.10.020>
 49. A. Munitz, R. Abbaschian, Liquid separation in Cu–Co and Cu–Co–Fe alloys solidified at high cooling rates, *Metall. Trans A*, 33 (1998) 3639-3649. doi: [10.1023/A:1004663530929](https://doi.org/10.1023/A:1004663530929)

50. L.F. Mondolfo, (1982) Grain refinement in casting and welds. In: Abbaschian R David S.A. (eds) TSM-AIME Warrendale, PA, p3.
51. A. Munitz, M. Bamberg, A. Venkert, P. Landau, R. Abbaschian, Phase selection in supercooled Cu-Nb alloys, J. Mater. Sci., 44 (2009) 64-73. [doi:10.1007/s10853-008-3115-y](https://doi.org/10.1007/s10853-008-3115-y).